IRAQI BULLETIN OF GEOLOGY AND MINING (IBGM)\
IRAQ GEOLOGICAL SURVEY (GEOSURV-IRAQ)

*IBGM (**2025**, Vol 21; Issue 2)* *203-231*

CRUSTAL STRUCTURE ANALYSIS BENEATH CENTRAL IRAQ USING RECEIVER FUNCTION (SHEAR WAVE VELOCITY)

Taif Qusay[1]*, and Najah Abd[1]

[1] Geology, Sciences, University of Baghdad, Baghdad, Iraq,
* Correspondence e-mail: Taif.Qassi1608a@sc.uobaghdad.edu.iq

Type of the Paper (Article)
Received: 07/04/2025
Accepted: 22/06/2025
Available online: 27/12/2025

Abstract

The Earth's crustal structure knowledge is essential to the advancement of geological comprehension and the refinement of seismic hazard analysis. In this study, we investigate the crustal structure beneath the seismographic stations in the Middle of Iraq using the receiver function (RF) technique. Seismological records were collected for Karbala (KAR2), Baghdad (BGD1), and Kut (KUT1) stations for the period January-December 2022. Earthquake event records of magnitude ≥6 Mw were collected from the European-Mediterranean Seismological Centre (EMSC). Data pre-processing was carried out for noise removal, instrument correction, and rotation of waveforms into a suitable coordinate system. Detection of seismic wave conversions at subsurface discontinuities, i.e., the Conrad and Moho boundaries, was achieved using the RF method with an iterative time-domain deconvolution algorithm. Crustal thickness and Vp/Vs ratio were estimated by the H-κ stacking method, and the rftn96 inversion tool sharpened the shear wave velocity (Vs) model. The results indicate strong crustal differentiation across the study region. On BGD1 (Baghdad station), the crust comprises 8 km of sedimentary cover with a P-wave velocity (Vp) of 4.1569 km/s, while the Moho is at a depth of 49 km, where Vp is 7.3554 km/s. The KUT1 station has 6 km of sediments (Vp = 5.0694 km/s) and a Moho depth of 52 km (Vp = 7.0152 km/s). The KAR2 station has a well-defined structure with 10 km of sediments (Vp = 4.3068 km/s) and a Moho depth of 40 km (Vp = 7.5624 km/s).

Keywords: Receiver functions; Crustal structure; Shear wave velocity; Vp/Vs analysis; Iraq.

1. Introduction

The structure of the Earth has been explored for over two centuries, primarily through the analysis of seismic waves generated within the Earth. These seismic waves reveal the Earth’s internal structure, which is stratified based on the chemical composition of its materials. The

ISSN 1811-4539, EISSN 3005-3714
https://doi.org/10.59150/ibgm2102a11
IBGM: http://ibgm-iq.org/
Academic Scientific Journals: www.iasj.net

Earth is divided into three main layers: the crust, the mantle, and the core (Jansson 2008). The crust varies in thickness, ranging from 35 km to 70 km on continents and approximately 5 km to 10 km under ocean basins. Beneath the crust lies the mantle, a 2,900 km thick layer that is separated into two parts, which are the upper mantle and the lower mantle. The core consists of two distinct parts: the outer core and the inner core, which are about 2,300 km and 1,200 km thick, respectively. The inner core is solid and predominantly composed of iron, making it the densest part of the Earth (Linang 2023; Pant 2015). A crucial boundary in the receiver function (RF) method is the one between the Earth's crust and mantle, known as the Mohorovičić discontinuity (Moho). Discovered in 1909 by Croatian seismologist Andrija Mohorovičić, this boundary varies significantly in depth depending on whether it lies beneath oceanic or continental crust. Under the ocean floor, the moho is typically found at depths ranging from 5 to 10 km. In contrast, beneath the continental crust, it ranges from 20 to 70 km, with an average depth of about 35 km (Torsvik 2015).

Therefore, analyzing the Earth's interior structure is critical for advancing geological knowledge and improving seismic hazard assessments. Traditional techniques such as seismic refraction, reflection, gravity, and geomagnetic investigations have been used for analysis, which have produced vital data and knowledge regarding the structures of the Earth's crust and upper mantle (Huda Farhan Rafea, Al-Heety, and Abdulnaby 2022). However, these techniques are often expensive and difficult, and involve extensive logistical assistance and comprehensive modeling of the periods and amplitudes of crustal body waves. Given the difficulties posed by traditional methods, the RF approach has shown superior performance in investigating the structure of the crust and upper mantle beneath seismic stations, overcoming these difficulties (Ortega and D'Auria 2022). The analysis of seismic waveforms recorded during distant earthquakes using the RF approach has provided valuable insights into earth discontinuities, such as Conrad and Moho discontinuities, which are difficult to detect using other methods (Vervaet and Darbyshire 2022).

The Mesopotamian Seismological Network (MPSN) is a regional broadband seismic network in Iraq, comprising 13 seismic stations deployed at various times since 2007 in several Iraqi cities, as shown in Figure 1. The network has been developed in cooperation and with the assistance of several institutions, such as the National Science Foundation (NSF), the U.S. Department of Energy (USDOE), and the University of Arkansas at Little Rock (UALR). It is managed by the Basrah Seismological Laboratory (SLUB), which was created in 2014 at the Department of Geology, College of Science, University of Basrah. SLUB is the MPSN's primary data center, in charge of collecting, reformatting, and archiving digital seismic data for all broadband stations. MPSN is used to monitor the seismicity of Iraq, especially close to the seismically active Zagros Fold Belt, and to supply essential data for geological and seismic hazard studies. The International Federation of Digital Seismograph Networks (FDSN) allocated the code MP to the Mesopotamian Seismological Network and incorporated it into the global seismological observing system (Asmaa N Al-Jabory and Abdulrahman 2024; Asmaa Najim Al-Jabory and Al-Heety 2024).

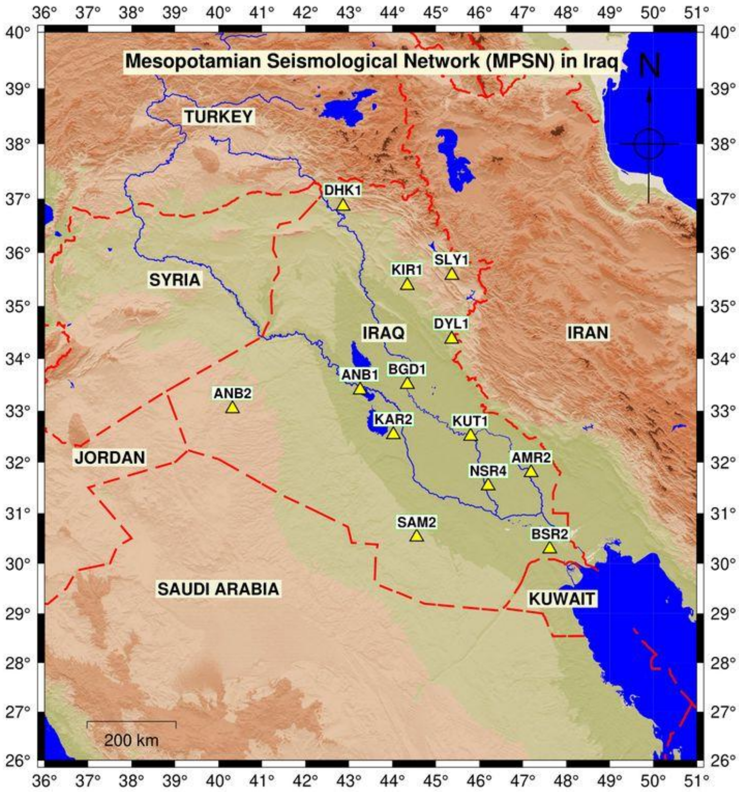

Figure 1. Map of Iraq and surrounding countries showing the Mesopotamian Seismological Network (MPSN) seismic stations.

Iraq, located in the northern part of the Arabian plate, is close to a subduction zone with the Iranian part of the Eurasia plate that exhibits considerable geological complexity and seismic activity. Central Iraq is notably affected by the tectonic interactions of these plates, resulting in a varied crustal composition. To the northeast of Iraq, the Zagros Fold Belt, which results from the convergence of the Arabian and Persian tectonic plates, is distinguished by significant folding, faulting, and crustal thickening. Further to the west, the old and sturdy Arabian Shield starkly contrasts with the more geologically dynamic Zagros area. Between these two prominent tectonic provinces, the Mesopotamian Foredeep is loaded with substantial sedimentary strata that further complicate the underlying structure (Fouad 2015; Sissakian, Abdullah, and Ghafur 2024). Even with this geological intricacy, comprehensive investigations of the subsurface under seismic stations in middle Iraq are few, leading to a considerable deficiency in comprehending the region's crustal characteristics, seismic waves transmission behavior, and tectonic processes. The absence of knowledge presents difficulties for several areas of information, such as seismic hazard evaluation, development of natural resources, and comprehending the fundamental tectonic processes that influence the area (Huda Farhan Rafea, Al-Heety, and Abdulnaby 2022) (Ghalib et al. 2008).

Recent studies have employed RF analysis to study mantle and crustal characteristics in various locales. Significant differences in crustal thickness, Vp/Vs ratios, and low-velocity zones are shown by these studies, providing important new information on geological development, lithospheric composition, and tectonic activity. Gök et al. (2008) performed a joint inversion of Rayleigh wave dispersion curves and P-wave RFs to provide an estimate of the crustal structure at two stations in Iraq (BGD (Baghdad) and MSL (Mosul) stations). They applied iterative deconvolution and H–κ stacking techniques to split the Ps conversions and surface wave data for constraints on shear-wave velocities. Their results showed crustal thicknesses of 43 km at BHD and 39 km at MSL, with 6 – 8 km and 2 – 4 km sedimentary thicknesses, respectively. They recorded a distinct Moho at BHD and a transitional Moho at MSL, reflecting active crustal thickening in the Zagros Fold Belt. Abdulnaby et al. (2012) studied the crustal structure under Duhok, north of Iraq, through a joint inversion of RFs and surface wave dispersion. The data of the Duhok broadband seismological station (DHK1, Fig. 1), which has been operating since 2007, were analyzed through four techniques: H-K stacking, surface wave dispersion inversion, RF inversion, and joint inversion. The joint inversion, combining RFs from 16 teleseismic events and Rayleigh wave group velocity dispersion from 20 regional events, provided the most accurate results. Their results revealed a 4 km sedimentary layer, a 16 – 18 km Conrad discontinuity, and a 40 – 42 km Moho discontinuity, indicating a 36 – 38 km crystalline crust thickness. Ramthan et al. (2020) employed P-wave RF to analyze seismic data from the NSR1 seismic station in Al-Refaei, Iraq, between June 2014 and July 2017. Nine teleseismic events with magnitudes greater than 6 Mw were chosen for analysis. Deconvolution methods were used to compute RFs that isolate the near-receiver structure and remove the effects of nearby source structures, followed by RF inversion using the rftn96 software. Their findings showed a crustal thickness of nearly 46 km, with an upper sedimentary sequence of 8 km thick. Abdulnaby et al. (2020) investigate Iraq's crustal structure using S-wave velocity modeling based on data from 12 seismographs placed throughout the Mesopotamian Plain and the Zagros Fold-Thrust Belt. Through combined inversion of P-wave RFs and Rayleigh wave dispersion data, their analysis demonstrated the Moho deepening from the Arabian platform toward the Zagros with a prominent root structure beneath the eastern part of the Mesopotamian Plain caused by sedimentary load. An upper-mantle low-velocity zone beneath the Mesopotamian foredeep indicates a lithospheric mantle that is weakening, which provides new insight into the tectonic development of Iraq. Rafea et al. (2022) used high-magnitude earthquake data from November 2018 to August 2021 to analyze the crustal structure under the ANB1 seismic station in Western Iraq, utilizing teleseismic P-wave RFs. To isolate crustal and upper mantle influences, they computed RFs from nine earthquake events using a Gaussian filter to enhance signal quality and suppress noise, and then performed inversion to derive the crustal velocity model. Their result showed a crustal thickness of about 44 km, a sedimentary cover of around 12 km, and four distinct crustal discontinuities. Albakr et al. (2022) investigated the crustal structure of the Dhufriyah and Kumaite oil fields in southeast Iraq by analysing ambient seismic noise. They employed cross-correlation techniques on seismic data recorded over six months from three broadband seismic stations in Anbar, Karbala, and Amarah. Rayleigh wave dispersion curves were utilised to recover a high-resolution shear velocity model of the sedimentary cover and the underlying crustal layers. Three significant discontinuities were identified: an interface between the sedimentary layers at 4 km depth with Vs at 2.44 km/s, basement rock at 12 km with Vs at 3.17 km/s, and the Moho at 46 km with Vs at 3.87 km/s. The results estimate the sediments' thickness as 12 km and the continental crust as a maximum of 34 km. Ahmad et al. (2023) employed P-wave RFs to investigate the crustal structure beneath Sulaymaniyah, northeast Iraq, using SLY1 seismic station data from October 2015 to October 2021. The RFs were stacked and inverted using Rayleigh wave dispersion data. Their examination of 46 earthquakes with magnitudes > 7Mw detected a 6 km sedimentary layer and 48 km Moho depth, indicating a 42 km crystalline crust. Furthermore, they identified severe discontinuities at 20 km and 38 km, indicating upper, middle, and lower crust transitions. (Huda F Rafea, Al-Heety, and Abdulnaby 2023) analyzed the crustal structure beneath Iraq's ANB1 and KAR2 seismic stations from 2018 to 2021 using RF techniques. The crustal structure was isolated at the receiver by deconvolving vertical and radial teleseismic waveform components, and a Gaussian filter was applied to eliminate high frequencies. The RFs were then inverted with an initial S-wave velocity model and processed using the rftn96 software. Their findings revealed a crustal thickness of 44 – 46 km in the western Mesopotamian Plain and an average Vp/Vs ratio of 1.79, indicating a distinct crustal composition. The primary contribution of this paper is to provide a comprehensive analysis of the crustal structure beneath the Baghdad (BGD1), Karbala (KAR2), and Kut (KUT1) seismic stations using the RF technique.

2. Theoretical Foundation of Receiver Function

RFs, a time series calculated from three-component seismograms, describe the Earth's structural reaction near the receiver. These responses are the consequence of the diverse trajectories that waveforms generated by teleseismic waves follow. Depending on the layers' material properties and the incidence angle, the energy of a body wave traveling through the Earth is transmitted, reflected, and potentially converted when it encounters an interface, such as the boundary between different layers (Ryan et al. 2016). Moho is a frequently encountered interface that serves as the boundary between the Earth's crust and mantle. Most energy remains as a transmitted P-wave when a P-wave (primary wave) ascends through the mantle and reaches the Moho. At the same time, a small portion of it transforms into an S-wave (secondary wave). These waves are captured at the earthquake stations and manifest in the RF as the Direct P-wave and the Ps phase, as shown in Figure 2. The RF technique does not consider the energy that is "lost" in the first waveform as P and S-waves that reflect into the mantle. Nevertheless, reflections from the free surface, the boundary between the Earth's crust and the atmosphere, are significant (Linang 2023)(ABERA 2016). A transmitted P-wave reflects at the free surface, generating multiples, including PpPs, PsPs, and PpSs. These signals reflect up from the Moho interface, as illustrated in Figure 2. These reflected and converted phases are essential for interpreting the Earth's subsurface structure using RFs (Wilson 2004).

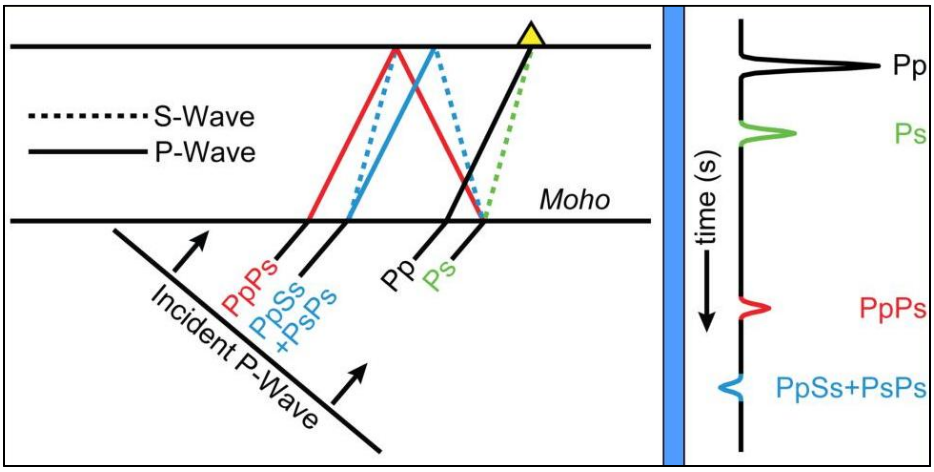

Figure 2. Analysis of Earth structure using RFs under a seismograph station (left). Isolation of wave arrivals and subsequent reverberations using RF (right) (Jansson 2008).

The RF approach is based on three fundamental concepts: the velocity disparity between P-waves and S-waves, multiples, and P-to-S conversion at the crustal boundary. To illustrate these ideas, consider a waveform that reaches an earthquake station above an individual layer, which represents the Earth's crust. Whenever P-wave impulses from distant seismic occurrences, such as earthquakes, reach the Moho, the barrier between the layers of the crust and mantle transforms part of them into S-waves (Ps). Due to their slower velocity, S-waves will take longer to cross the crust, leading to a delayed arrival at the seismic station compared to the straight P-wave. The depth of the Moho interface may be precisely determined by studying the difference in time to arrival across the initial P-wave and the converted Ps wave, and using a velocity model. Furthermore, the method utilizes multiple reflections of both P and S waves, such as PpPs, PsPs, and PpSs, which provide additional insights and redundancy, thereby improving the precision of subsurface calculations (Jansson 2008; Cassidy 1991). The RF approach's primary goal is to distinguish the near-receiver construction via the effects of the source and remote geological formations, thereby enabling more precise interpretations of the Earth's subsurface (Ryan et al. 2016).

A seismic station records an earthquake or near-source impact *S(t)*, together with the Earth's response function *E(t)*, the instrument response *I(t)*, and a time-dependent noise *n(t)*. This convolution is what makes up the seismic signal. Equations 1~3 describe the signals acquired by a three-component seismometer (vertical $X_Z(t)$, horizontal: radial $X_R(t)$, and transverse $X_T(t)$) (Linang 2023) (Cassidy 1991).

$$X_Z(t) = S(t) \times I(t) \times E_Z(t) + n(t) \quad 1$$

$$X_R(t) = S(t) \times I(t) \times E_R(t) + n(t) \quad 2$$

$$X_T(t) = S(t) \times I(t) \times E_T(t) + n(t) \quad 3$$

The P-to-S converted phases are recorded by the horizontal components of seismic motion, while the vertical component primarily captures the initial P-wave approach. This assumes that the seismic wave travels in a roughly vertical ray path underneath the receiver. For steeply incident waves, the Earth's vertical response, $E_Z(t)$, may be approximated by a basic delta function, as indicated in Equation 4. The convolution of the source signal *S(t)*, instrument response *I(t)*, and time-dependent noise *n(t)* can be used to simplify the vertical component of motion $X_Z(t)$ under these assumptions, as described in Equation 5 (Linang 2023; Cassidy 1991).

$$E_Z(t) = \delta(t) \quad 4$$

$$X_Z(t) \approx S(t) \times I(t) + n(t) \quad 5$$

The Earth response functions E_R and E_T can be isolated by deconvolving the vertical motion component from the radial or transverse motion components, which are termed radial and transverse RFs, as described by equations 6 and 7 (Linang 2023), where ω is the frequency of the angle, $E_R(\omega)$ and $E_T(\omega)$ are the Earth's radial and transverse response functions, $X_R(\omega)$, $X_T(\omega)$, and $X_Z(\omega)$ are the Fourier transforms of the radial, transverse, and vertical components, F denotes the Fourier transform; and $E_R(t)$, $E_T(t)$ are the time-domain Earth response functions. Radial RFs, which record P-to-SV (Primary to Secondary Vertical) wave mode conversions, are often used to examine the structure of radial discontinuities under a seismic station. Conversely, transverse RFs, mostly including SH (Shear Horizontal) wave motion, are advantageous for examining characteristics such as dipping layers and subsurface anisotropy (Liu and Niu 2012).

$$E_R(\omega) = \frac{X_R(\omega)}{X_Z(\omega)} = \frac{F(S(t) \times I(t) \times E_R(t))}{F(S(t) \times I(t))} \quad 6$$

$$E_T(\omega) = \frac{X_T(\omega)}{X_Z(\omega)} = \frac{F(S(t) \times I(t) \times E_T(t))}{F(S(t) \times I(t))} \quad 7$$

2.1. Deconvolution

Deconvolution is an essential technique in seismology, particularly for analyzing RFs. It aims to improve the clarity and resolution of seismic signals derived from distant earthquake events (Zhong and Zhan 2020). Various deconvolution techniques are often used in RF analyses, typically classified into time-domain and frequency-domain deconvolution. Time-domain deconvolution is often preferred due to its simplicity, since it does not require any particular parameterisation to stabilise the deconvolution process in the presence of noise. Nonetheless, it is often more computationally intensive than frequency-domain approaches, while it provides more flexibility and reduces the occurrence of side-lobes—artifacts resulting from the use of Fast Fourier Transforms (Torsvik 2015). The vertical and radial components of motion are connected through a convolutional relationship. Equation 8 illustrates the relation of the RF, $ERi\ (t)$, to the radial (R) and vertical (Z) components (Linang 2023).

$$R(t) = Z(t) * E_{R_i}(t) \quad 8$$

The iterative time-domain deconvolution method developed by Ligorría and Ammon (1999) was used to compute RFs for analyzing the structure of the crust and upper mantle. This approach was selected due to its simplicity, since it does not need the optimization of parameters (such as water-level, damping, or time-domain smoothing) often required in other deconvolution techniques. The fundamental computation objective of iterative time-domain deconvolution, as defined in equation 9, is to combine an iteratively updated spike with the vertical-component seismogram in order to minimize the discrepancy between the actual horizontal seismogram and the projected pulse (Ligorría and Ammon 1999). Concretely, the vertical component Z(t) is first cross-correlated with the radial component R(t) to determine the lag of the largest initial spike in the RF. Next, the convolution of the current RF estimate $E_{R_i}(t)$ and the vertical component seismogram is subtracted from the radial-component seismogram, as shown in equation 10. At each iteration, this operation reduces the residual between the radial data and the convolved RF. The iterations are continued until additional spikes no longer produce a substantial reduction in the misfit. The outcome is the RF with the estimated spike amplitudes and lags. The deconvolution process uses a Gaussian filter, which is described by Equation 11, where α is the filter's width. The Gaussian filter controls the spectral component of the RF, often reducing noise at higher frequencies (Linang 2023).

$$X_R(t) = X_Z(t) * E_R(t) + n(t) \quad 9$$

$$R(t) - E_{R_i}(t) * Z(t) \quad 10$$

$$G(\omega) = e^{\left(\frac{-\omega^2}{4\alpha^2}\right)} \quad 11$$

3. Materials and Methods

We analyze three stations in central Iraq, Baghdad (BGD1), Karbala (KAR2), and Kut (KUT1), through three essential phases: data collection, pre-processing, and RF analysis, as shown in Figure 3. During the data collection phase, continuous seismic data were gathered from the BGD1, KAR2, and KUT1 stations, in addition to collecting teleseismic earthquake events from the European-Mediterranean Seismological Centre (EMSC) source for earthquakes. During the pre-processing stage, several procedures were performed using the Computer Programs in Seismology (CPS) software package. These included converting GCF files to SAC format, incorporating event metadata, removing the instrument response, and rotating seismic data components from NEZ (north-south, east-west, and vertical) to ZRT (vertical, radial, and transverse). Following pre-processing, the seismic data is sent to the RF analysis stage, where the RF is calculated using the time domain iterative deconvolution technique. Then it is inverted using the initial velocity model and rftn96 tools, which employ a linear iterative inversion method to identify velocity discontinuities and subsurface structures. The final results are then plotted for interpretation.

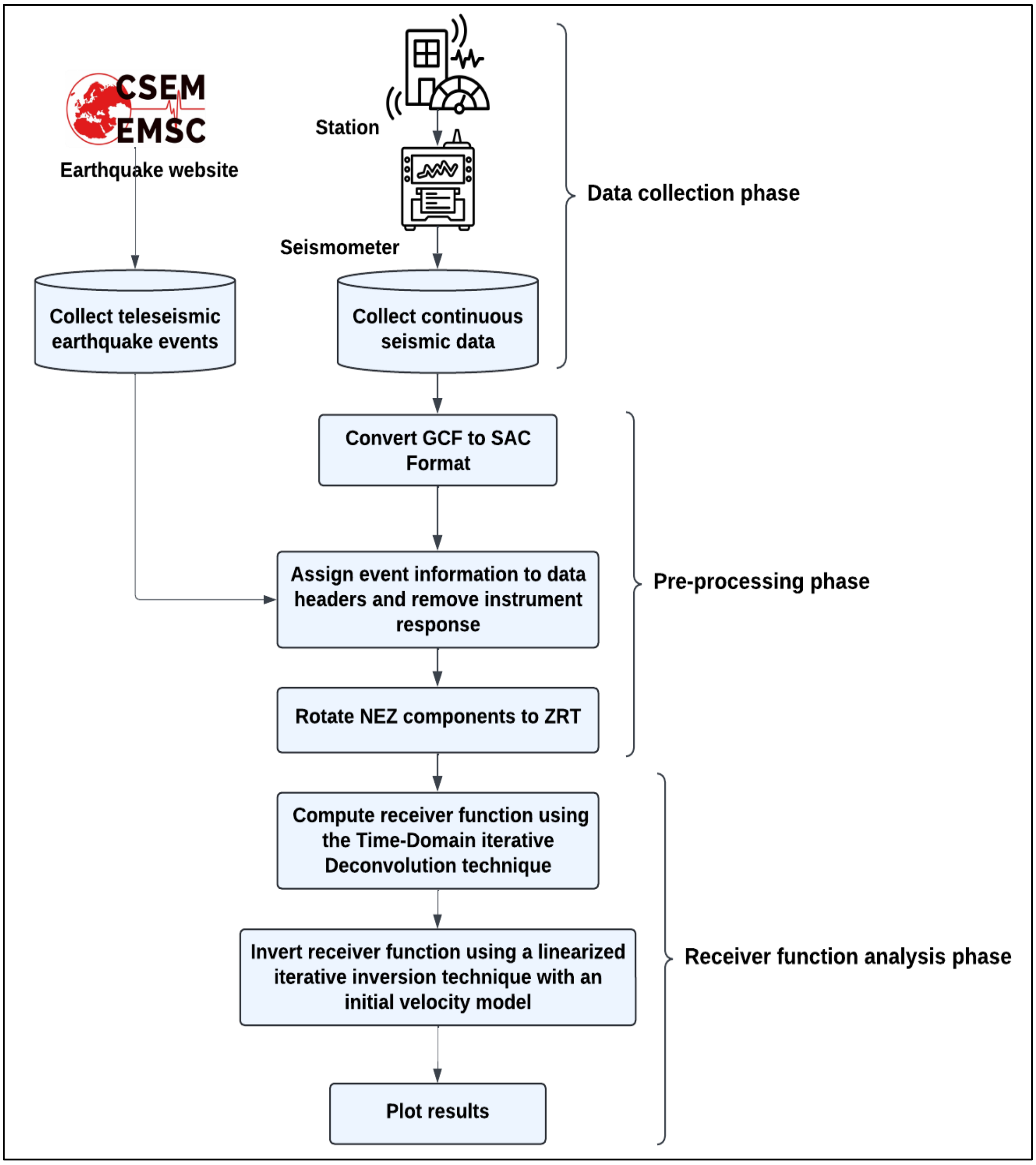

Figure 3. General method for crustal structure analysis beneath stations.

3.1. Data collection

The datasets were collected from the Kar2 and Kut1 stations using a Güralp device installed at each station, and from the BGD1 station using a Nanometrics device. The Güralp sensor stores seismic data hourly in the Güralp Compressed Format (GCF), whereas the Nanometrics sensor records data in the MiniSEED format, saving files once they reach a maximum size of 4000 KB. The data were recorded during the period from January 2022 to December 2022 in central Iraq, as shown in Figure 4a. The RF depends on a series of criteria that have to be satisfied in order to correctly picture the subsurface. One of these constraints is a high seismic magnitude, which assures a high signal-to-noise ratio across extended distances. To reach the required propagation channels, an earthquake must strike within 30 and 90 degrees, or at 180 degrees, from the seismic station. Therefore, the teleseismic earthquake events with a magnitude ≥ 6 and an epicentral distance between 30 and 90 degrees were selected from the Kar2 and Kut2 stations for RF analysis. The event information was obtained from the open-source EMSC. The data gathered comprises the location, time, magnitude, and depth of the analyzed events. A total of 246 teleseismic earthquake occasions were selected during the specified period of the data recorded at both the Kar2 and Kut1 stations, while 114 events were chosen during the specified period of the data recorded at the BGD1 station, as shown in Figure 4b. Appendix 1 presents a sample of the teleseismic events used in the RF analysis for the KAR2 and KUT1 stations. Similarly, Appendix 2 presents a sample of the teleseismic events analyzed for the BGD1 station. Both tables include details such as the event date, time, coordinates, depth, and magnitude.

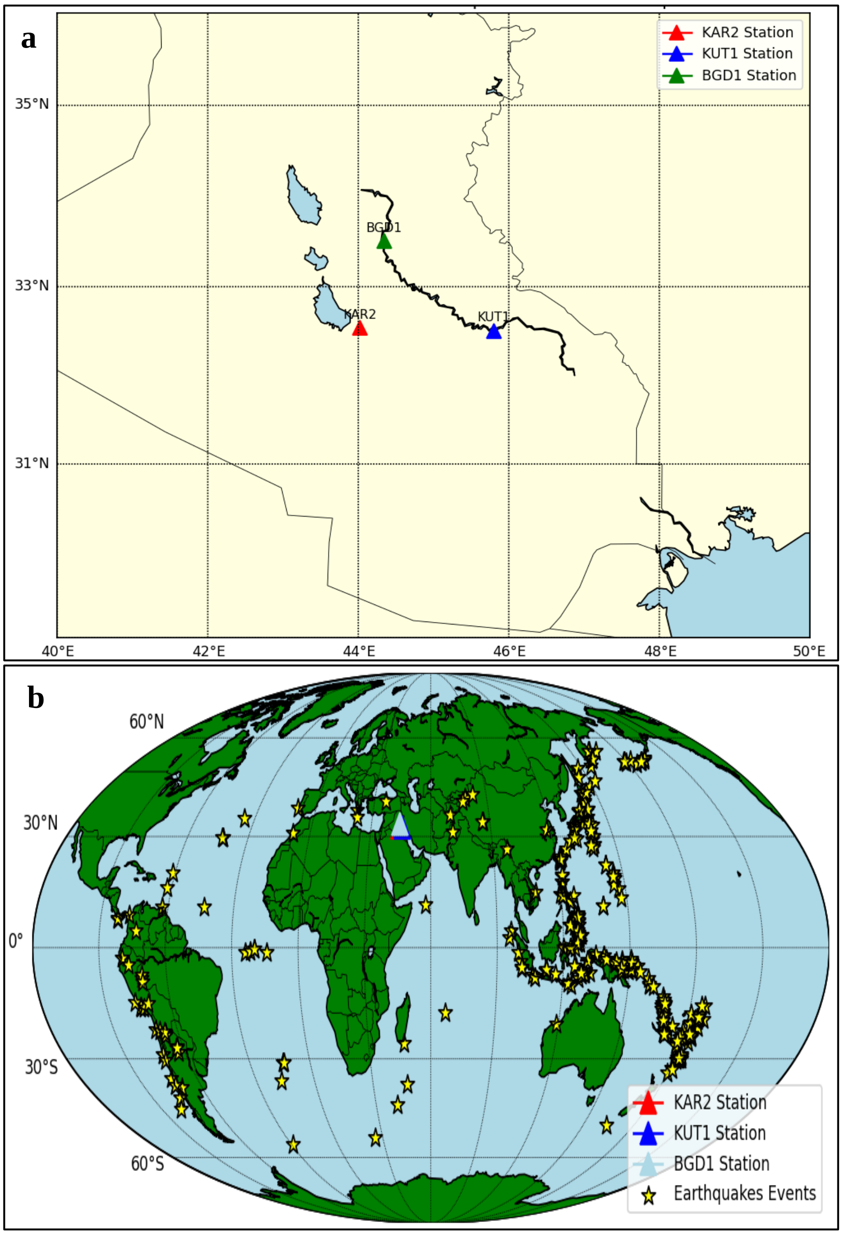

Figure 4. a) Location of stations, b) Location of selected teleseismic earthquake events.

3.2. Pre-processing

At this stage, the collected seismic data are pre-processed before passing through the RF analysis stage to remove noise and prepare waveforms. The pre-processing operations applied to the seismic data are described in the following:

a) **Converting GCF, MiniSEED to SAC Format:** The seismic data used in this study were originally provided in GCF (Güralp Compressed Format) for the KAR2 and KUT1 stations. These data were converted to SAC (Seismic Analysis Code) format using the gcf2sac conversion tool provided by IRIS (Trabant, 2013). This tool effectively transforms GCF waveform data into SAC format, supporting both ASCII and binary output. In contrast, the BGD1 station data were originally in MiniSEED format. These MiniSEED files were converted to SAC format using the mseed2sac utility from the ObsPy Python package. This function reads MiniSEED traces and outputs SAC files while preserving the original trace content, enabling seamless integration with SAC-based processing workflows.

b) **Instrument Response Removal and SAC Header Assignment:** Once the seismic data have been converted to SAC format, the next step is to remove instrument responses and assign SAC header values to ensure an accurate representation of ground motion. Removing the instrument response eliminates distortions introduced by the recording instruments, allowing the seismic count data to reflect true ground motion (Helffrich, Wookey, and Bastow 2013; Abdelwahed 2012). However, if the instrument responses of different components are already matched, removal may not be necessary. Nevertheless, it is essential to equalize the gains before proceeding with further analysis, such as RF deconvolution. Key seismic event information is then added to the SAC file headers, which store metadata describing the seismic trace and facilitate analysis. These headers include essential details such as event latitude, longitude, depth, timestamp, and magnitude, as well as information on signal characteristics, including time and sampling rate. This step is crucial for isolating the response of nearby receiver structures from distant sources, as seismic waves travel through different paths and media, carrying valuable information about the subsurface structure beneath the seismic station.

c) **Rotation of Seismic Components:** the three-component seismic data NEZ are then rotated into ZRT components using equation 12, where γ is the back azimuth (Torsvik 2015). By rotating the data, seismic wave components can be better separated, improving the understanding of wave propagation. This process helps map geological discontinuities and anisotropies, providing insights into the Earth's subsurface. It also enhances polarization analysis and improves data quality and instrument correction by aligning recorded signals with their true propagation paths, ensuring more accurate seismic interpretation (Ariyanto et al. 2020). Figure 5 represents an example output of seismic component rotation from NEZ to ZRT, showing radial and transverse signals (R, T) for different filter ranges.

$$\begin{bmatrix} R \\ T \\ Z \end{bmatrix} = \begin{bmatrix} -\cos\gamma & -\sin\gamma & 0 \\ \sin\gamma & -\cos\gamma & 0 \\ 0 & 0 & 1 \end{bmatrix} \begin{bmatrix} N \\ E \\ Z \end{bmatrix} \quad 12$$

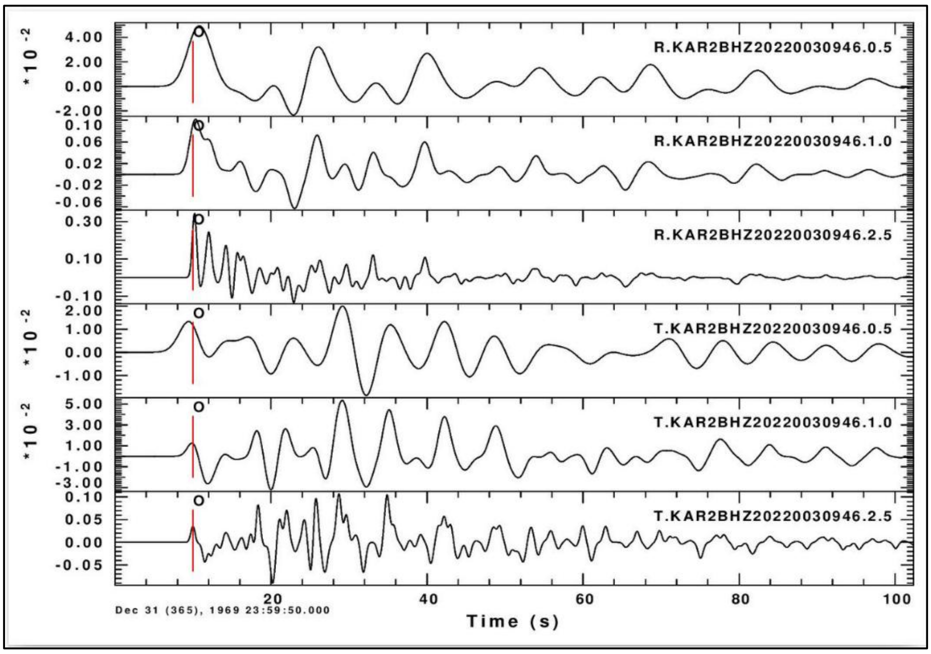

Figure 5. Example output of seismic component rotation from NEZ to ZRT.

3.3. Processing (Computation of RF)

3.3.1. Deconvolution

Information regarding the event's source, trajectory through the mantle, and the specific subsurface structure beneath the station is obtained from the teleseismic waves that reach the broadband seismic station. The RF technique attempts to define the crustal structure at the receiver by removing the impacts of the source's crustal structure and remote structural influences (Huda F Rafea, Al-Heety, and Abdulnaby 2023). The time domain iterative deconvolution approach (Ligorría and Ammon 1999) was used in this work to conduct the RF in order to remove the influence of neighboring source structures and source time functions. The procedure commences with manually identifying the P wave's arrival from preprocessed seismic data utilizing the GSAC tool. After placing the P-wave arrival, the data were subjected to high-pass and low-pass filters to minimize noise and avoid aliasing, guaranteeing the RF's stability. The radial and transverse components of the seismic data were then used as input for the iterative deconvolution procedure, which was carried out over 30 iterations to calculate the RF at various Gaussian weights (0.5, 1.0, and 2.5). The deconvolution method systematically eliminates the source wavelet, repeatedly refining the starting model according to the observed data. With each iteration, the alignment between the observed data and the modeled response improves, reducing residual errors and increasing the accuracy of the RF.

We obtained RFs with a deconvolution accuracy exceeding 80%. Figure 6 represents an example output of the deconvolution process.

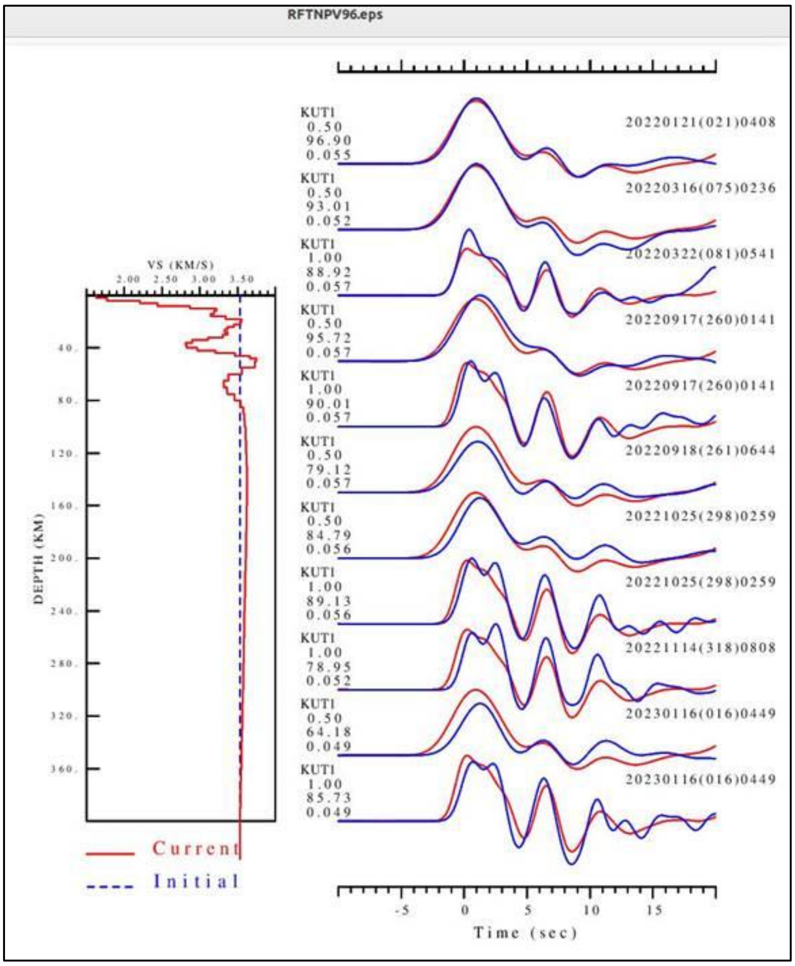

Figure 6. Example output of the deconvolution process.

3.3.2. Stacking

After the deconvolution process and obtaining RFs, we applied the H-k stacking method to stack the RFs. The H-k stacking technique, developed by Zhu and Kanamori (2000) (Zhu and Kanamori 2000), is one of the common methods in determining crustal thickness and the bulk crustal VP/VS ratio using teleseismic RFs. The amplitude sum of the P-to-S conversions beneath a seismic station is maximised by the optimal combination of Moho depth (H) and VP/VS ratio (k). This method assumes that the Moho has the most pronounced velocity contrast, resulting in the most extensive P-to-S conversion and concomitant reverberation phases. In order to maximize the linear stack function s(H,k), which is defined by equation 13, the method conducts a grid-based examination of potential H and k values using the estimated times of arrival of Moho-converted instances (Ps, PpPs, and PsPs + PpSs). Where stacking weights are represented by w_1 w_2 and w_3, The RF amplitudes at the predicted arrival times of the P-to-S conversion (Ps) and reverberations (PpPs and PsPs + PpSs) are represented by $r_j(t_i)$, and N is the total number of RFs used to increase the signal-to-noise ratio (SNR). The predicted travel time for each phase t_i is obtained by equations 14, 15, and 16, where p is the ray parameter (Linang 2023).

$$s(H,k) = \sum_{j=1}^{N} w_1 r_j(t_1) + w_2 r_j(t_2) + w_3 r_j(t_3) \quad 13$$

$$t_1 = H\left[\sqrt{\frac{1}{V_S^2} - p^2} - \sqrt{\frac{1}{V_P^2} - p^2}\right] \quad 14$$

$$t_2 = H\left[\sqrt{\frac{1}{V_S^2} - p^2} - \sqrt{\frac{1}{V_P^2} - p^2}\right] \quad 15$$

$$t_3 = 2H\sqrt{\frac{1}{V_S^2} - p^2} \quad 16$$

3.4. Inversion of RF

The RF approach uses data from seismic stations to produce a time series that illustrates velocity fluctuations inside various levels of the Earth's structure. This technique emphasizes phase arrivals near seismic discontinuities, such as the Moho, and translates these arrival times into depth estimations. Understanding the seismic velocities in the Earth's strata is necessary for iterative inversion, which transforms seismic phases into depths. Variations in S-wave velocity and the existence of velocity discontinuities are essential in influencing RFs, facilitating the identification and mapping of subsurface structures such as the crust-mantle boundary and other significant geological features (Abdulnaby, Mahdi, and Al-Shukri 2012) (Ahmad and Abdulnaby 2023). A homogeneous earth structure model called a half-space, starting with an S-wave velocity (Vs) of 4.04 km/sec, was used to invert the obtained RF results. The velocity model used in this inversion consists of 45 layers extending to a depth of 400 km. The first 10 layers represent the upper crust, which ranges from 0 to 20 km and has a thickness of 2 km per layer. The other 15 Layers constitute the middle crust with a depth range of 20 – 50 km, with each layer having a thickness of 2 km. Layer 26 represents the boundary between the crust and upper mantle at a depth of 50 km. The other nine layers represent the transition from the lower crust to the upper mantle with depths ranging from 50 – 100 km and a thickness of 5km per layer. Nine layers represent the upper mantle with a depth extending from 100 km to 400 km and a thickness of 10 km per layer. Finally, layer 45 defines the lowest layer and often signifies the limit of the lower mantle or the transition zone. In an effort to identify sudden velocity discontinuities throughout the inversion process, this model is designed to be impartial and proficient. The inversion was executed via the rftn96 tool inside the CPS(Computer Programs in Seismology) package, where it employs a linearized iterative inversion technique that modifies an initial velocity model to reduce the discrepancy between the observed RFs (obtained from seismic data) and the predicted RFs (Computed from the starting velocity model). The inversion for each seismic event was conducted over twelve iterations to get the RFs. After the inversion process, we retained only the events with a fit accuracy greater than 74 and removed entirely any events below this accuracy.

4. Results and Discussion

4.1. Assessment of RF Stacking and Inversion Performance

The RFs are shown in Figure 7, which are represented as a back azimuth for the chosen seismic events, in the range of 30º to 90º for three stations: BGD1, KAR2, and KUT1. The back azimuth analysis helps determine whether seismic events were aligned or deviated. The red areas represent positive amplitude arrivals, which indicate velocity contrasts within the Earth's crust. Differences in waveform complexity and arrival times between the stations suggest variations in crustal structure and thickness at each location.

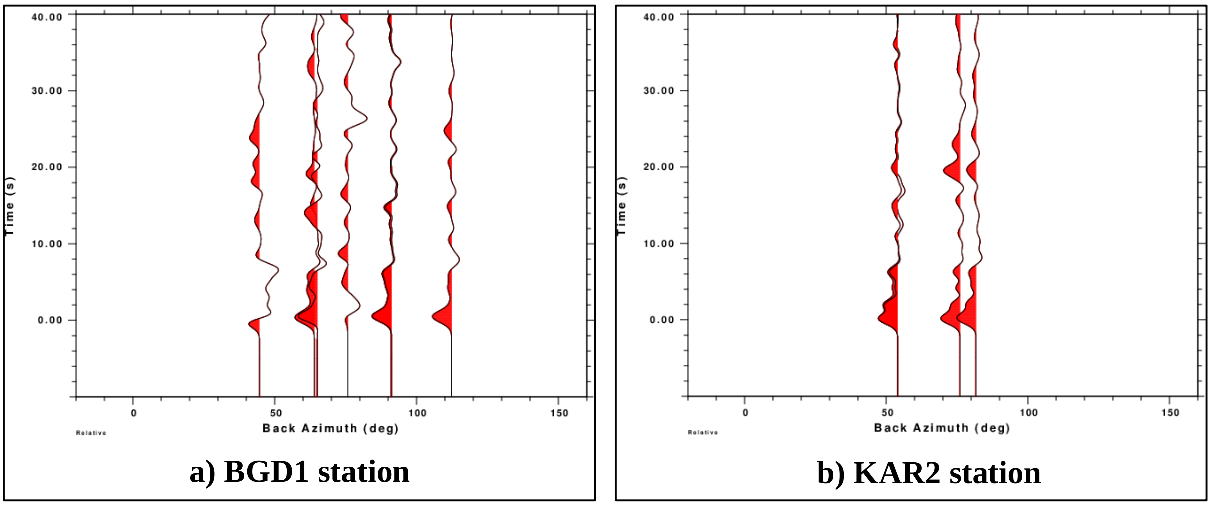

Figure 7. Back-Azimuth stacking of RFs for BGD1, KAR2, and Kut1 Stations.

The crustal velocity structure under each station was obtained through the inversion of RFs, with ten RFs being used for the BGD1 station, six for the KAR2 station, and nine for the KUT1 station. Figure 8 illustrates the velocity model that best fits the RF. There is a 67% to 96% spread in the quality of the fit between the measured RF (blue) and the model forecast (red) when Alpha is between 0.5 and 1.

The shear wave velocity (Vs) and Q inverse and normalized resolution matrices models for three stations are shown in Figure 9. In the left panel of the Vs and Q inverse model, the red dashed lines represent the initial velocity model for the current iteration, while the blue solid lines indicate the updated model after the most recent inversion step, highlighting the improvement achieved through the inversion process. The right-hand panel shows the normalized resolution matrix, which measures the reliability and accuracy of the velocity model at different depths. In all cases, a damping factor of 0.5 was chosen based on trial inversions because it provided the best balance between model smoothness and data fit by minimizing instability while preserving important structural features.

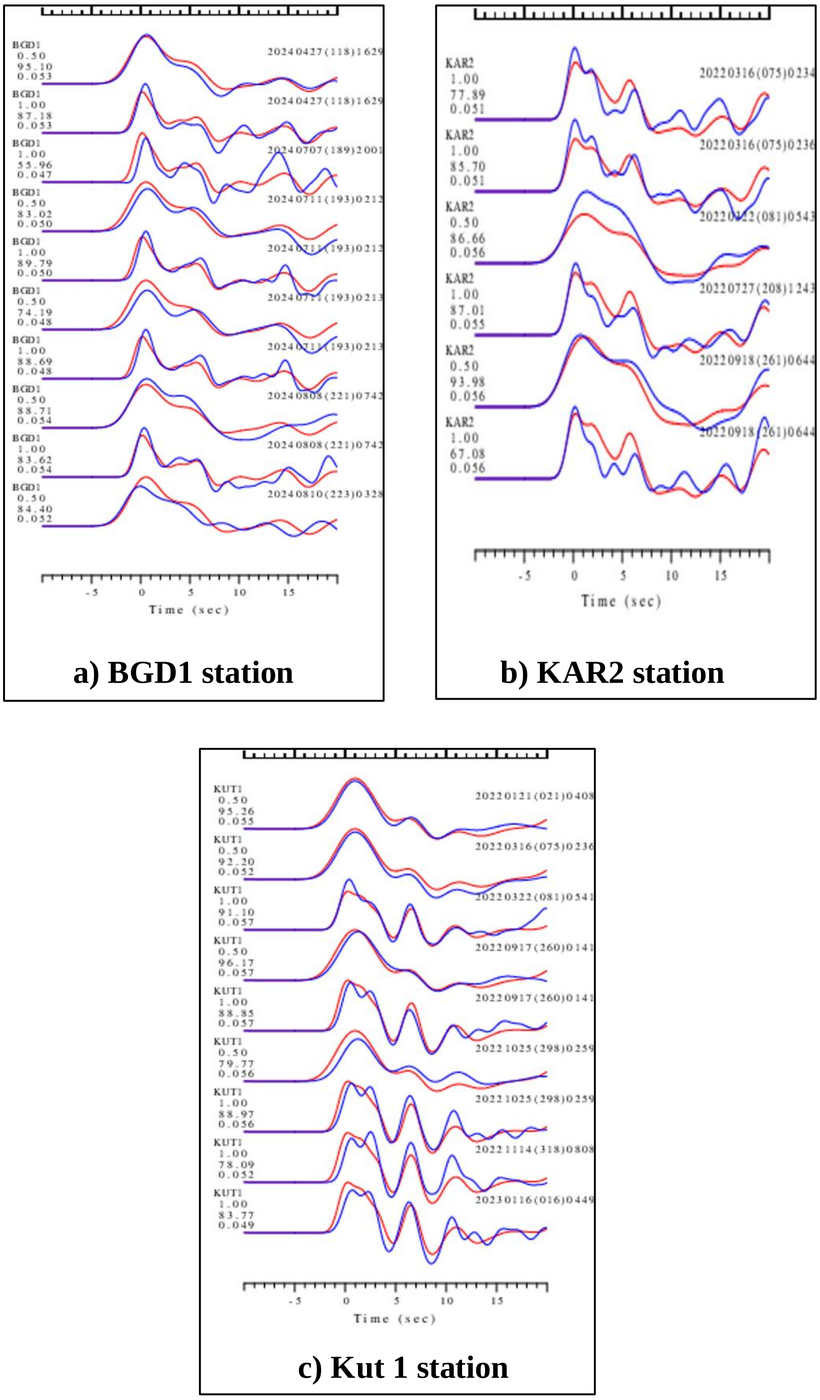

Figure 8. Model Fit to RFs. The blue curve represents the observed data, while the red curve corresponds to the model prediction. Each RF is labeled on the left with the station name, Alpha (Gaussian filter parameter), percentage of fit, and ray parameter (sec/km). The upper right of each trace provides the event date and time (year/month/day/hour/minute). A time scale is included at the bottom of the figure.

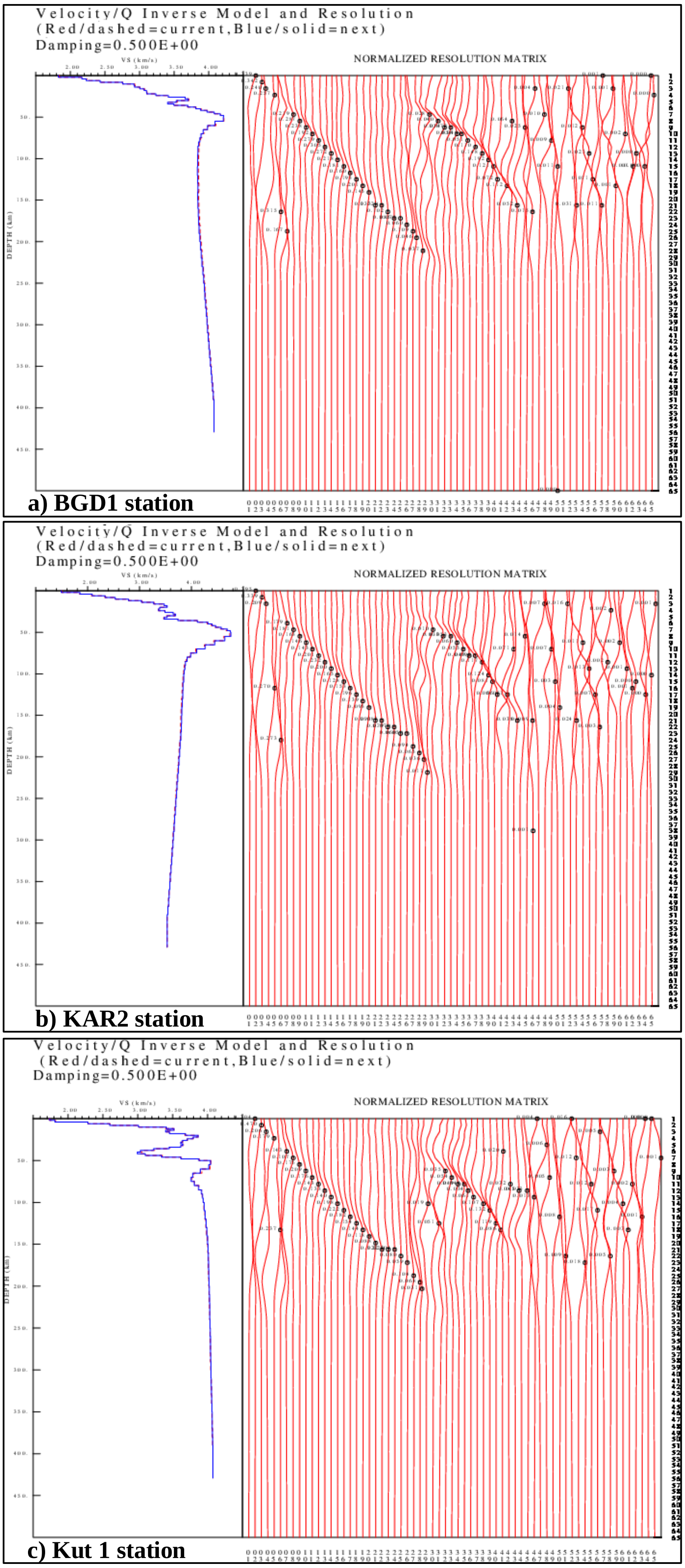

Figure 9. Velocity and Q inversion model with resolution matrices for BGD1, KAR2, and KUT1 stations.

4.2. Crustal Thickness and Velocity Structure

The crustal velocity model beneath the KAR2, BGD1, and KUT1 seismic stations, established via RF inversion, consists of three layers: the sedimentary cover, the upper crust, and the lower crust. The velocity model shows two important earthquake discontinuities: the Moho discontinuity marks the boundary between the crust and the mantle, and the Conrad discontinuity splits the upper and lower crust.

The crustal velocity model beneath the KAR2 station is listed in Table 1 and illustrated in Figure 10. The crust beneath the KAR2 station exhibits a layered structure extending to a Moho depth of approximately 40 km. A sedimentary layer spans the top 10 km, underlain by the upper crust reaching 20 km. The Conrad discontinuity, separating the upper and lower crust, is identified at around 26 km depth, while the lower crust extends to 34 km. The transition to the upper mantle is marked by the Moho, indicating a significant increase in seismic velocities and density, consistent with typical continental crustal structures.

The crustal velocity model for station BGD1, as described in Table 2 and shown in Figure 11, reveals a total crustal thickness of approximately 49 km. The sedimentary layer is relatively thin, extending to about 8 km, followed by an upper crust reaching a depth of 19 km. The Conrad discontinuity is identified at 26 km, marking the transition to the lower crust, which continues to around 37 km. The Moho boundary at 49 km depth represents a significant structural change, indicating deeper crustal development beneath this station.

Table 1. Crustal architecture beneath KAR2 from RF analysis.

RHOB (g/cm^3)	Vs (km/sec)	Vp (km/sec)	Depth (km)	Layer
2.43	2.53	4.30	10	Sedimentary cover
2.72	3.53	6.01	20	Upper crust
2.70	3.48	5.93	26	Conrad
2.69	3.47	5.89	34	Lower crust
3.14	4.32	7.56	40	Moho

Table 2. Crustal architecture beneath BGD1 from RF analysis.

RHOB (g/cm^3)	(Vs km/sec)	Vp (km/sec)	Depth (km)	Layer
2.41	2.42	4.15	8	Sedimentary Thickness
2.57	3.10	5.22	19	Upper crust
2.67	3.41	5.80	26	Conrad
2.79	3.69	6.33	37	Lower crust
3.07	4.21	7.35	49	Moho

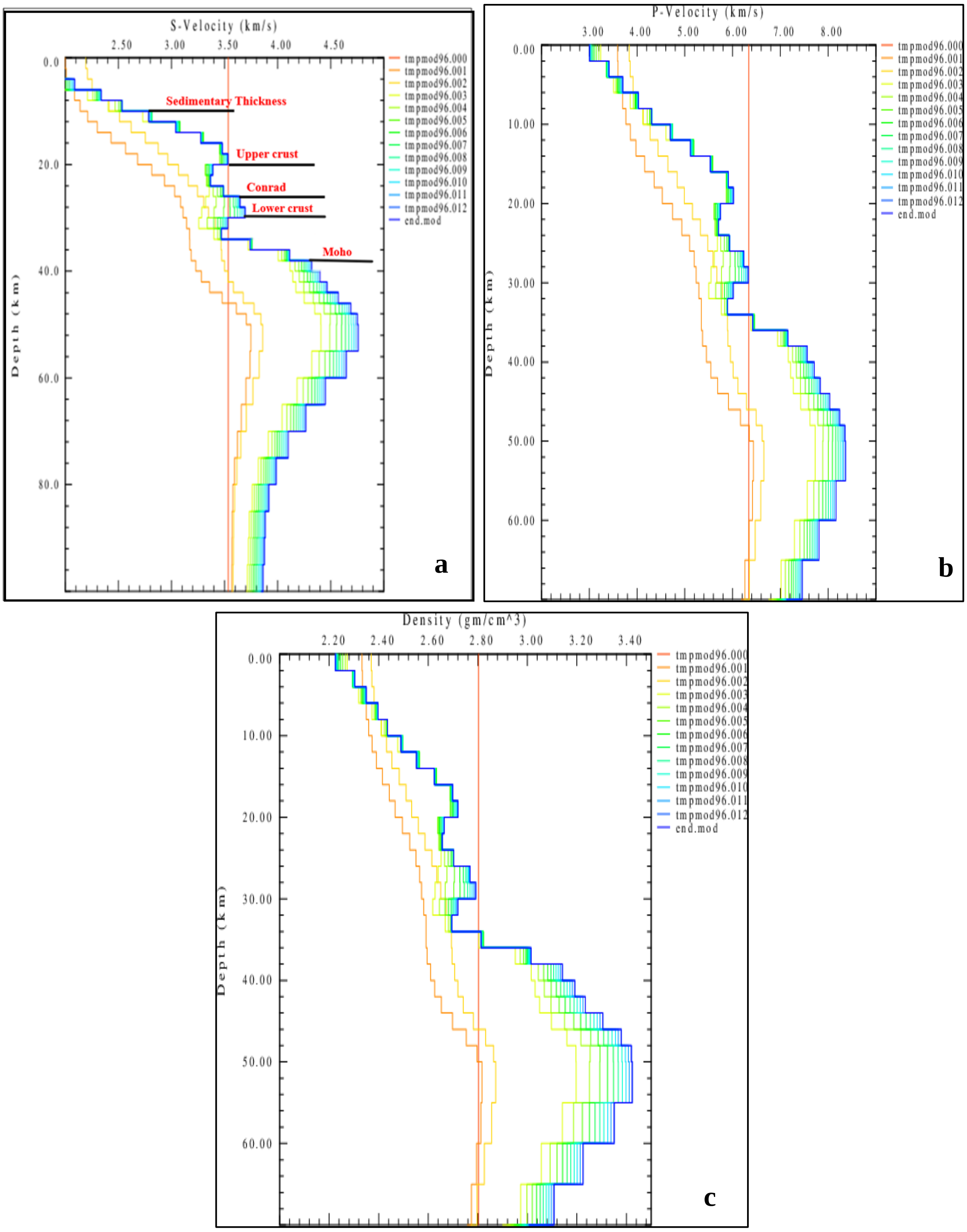

Figure 10. Crustal velocity model beneath the KAR2 station based on RFs: (a) S-wave velocity, (b) P-wave velocity, and (c) density profile.

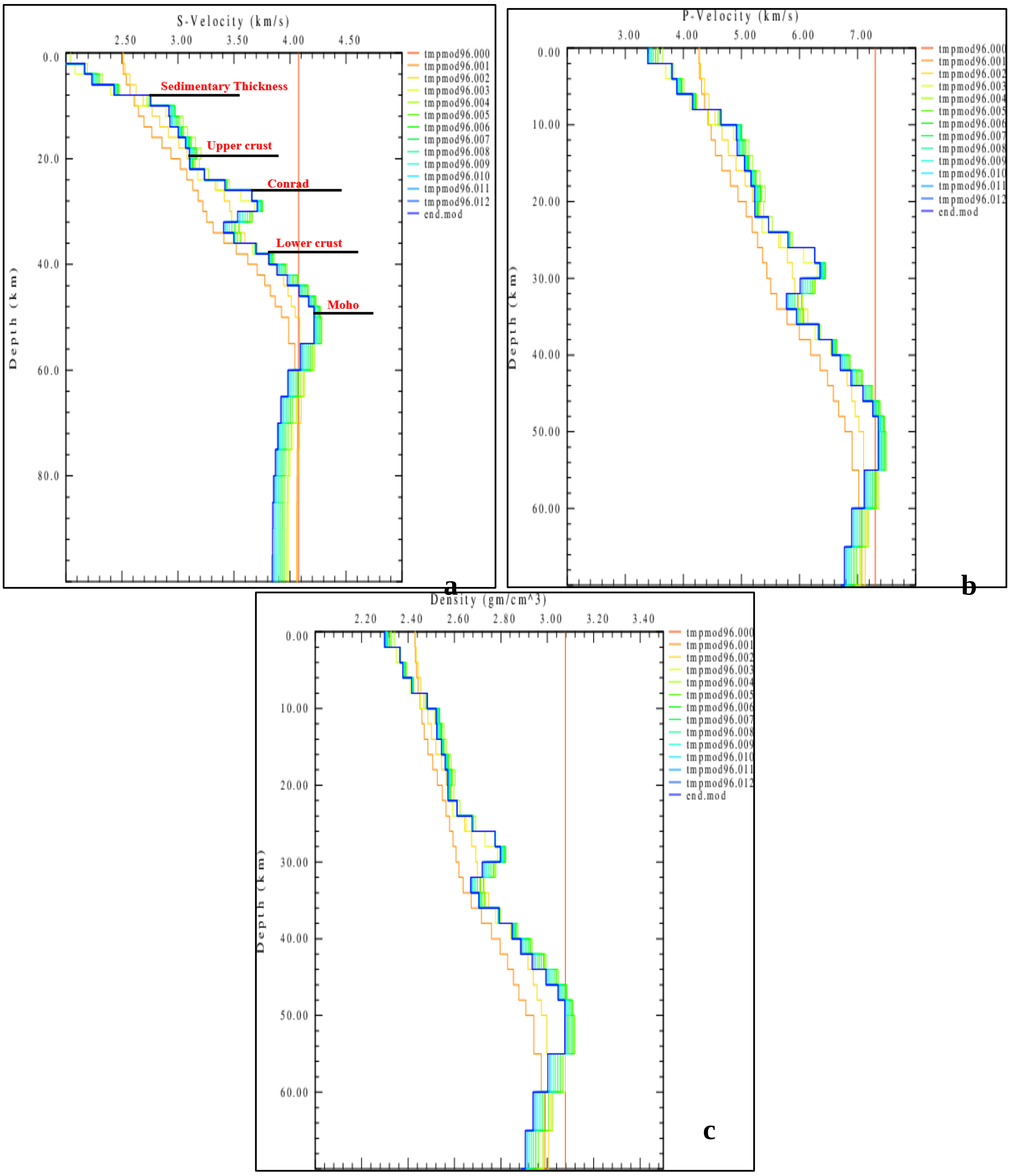

Figure 11. Crustal velocity model beneath the BGD1 station based on RFs: (a) S-wave velocity, (b) P-wave velocity, and (c) density profile.

On the other hand, the crustal velocity model beneath the KUT1 station, as listed in Table 3 and shown in Figure 12, indicates a total crustal thickness of approximately 52 km. The sedimentary layer extends to 10 km, followed by an upper crust reaching 18 km depth. The Conrad discontinuity is identified at 33 km, marking the transition to the lower crust, which continues to around 46 km. The Moho boundary at 52 km depth reflects a distinct crust–mantle transition, suggesting a thicker and more developed crustal structure beneath this station.

Table 3. Crustal architecture beneath KUT1 from RF analysis functions.

RHOB (g/cm^3)	Vs (km/sec)	Vp (km/sec)	Depth (km)	Layer
2.54	3.01	5.06	10	Sedimentary Thickness
2.68	3.45	5.86	18	Upper crust
2.75	3.61	6.17	33	Conrad
2.64	3.33	5.65	46	Lower crust
2.97	4.04	7.01	52	Moho

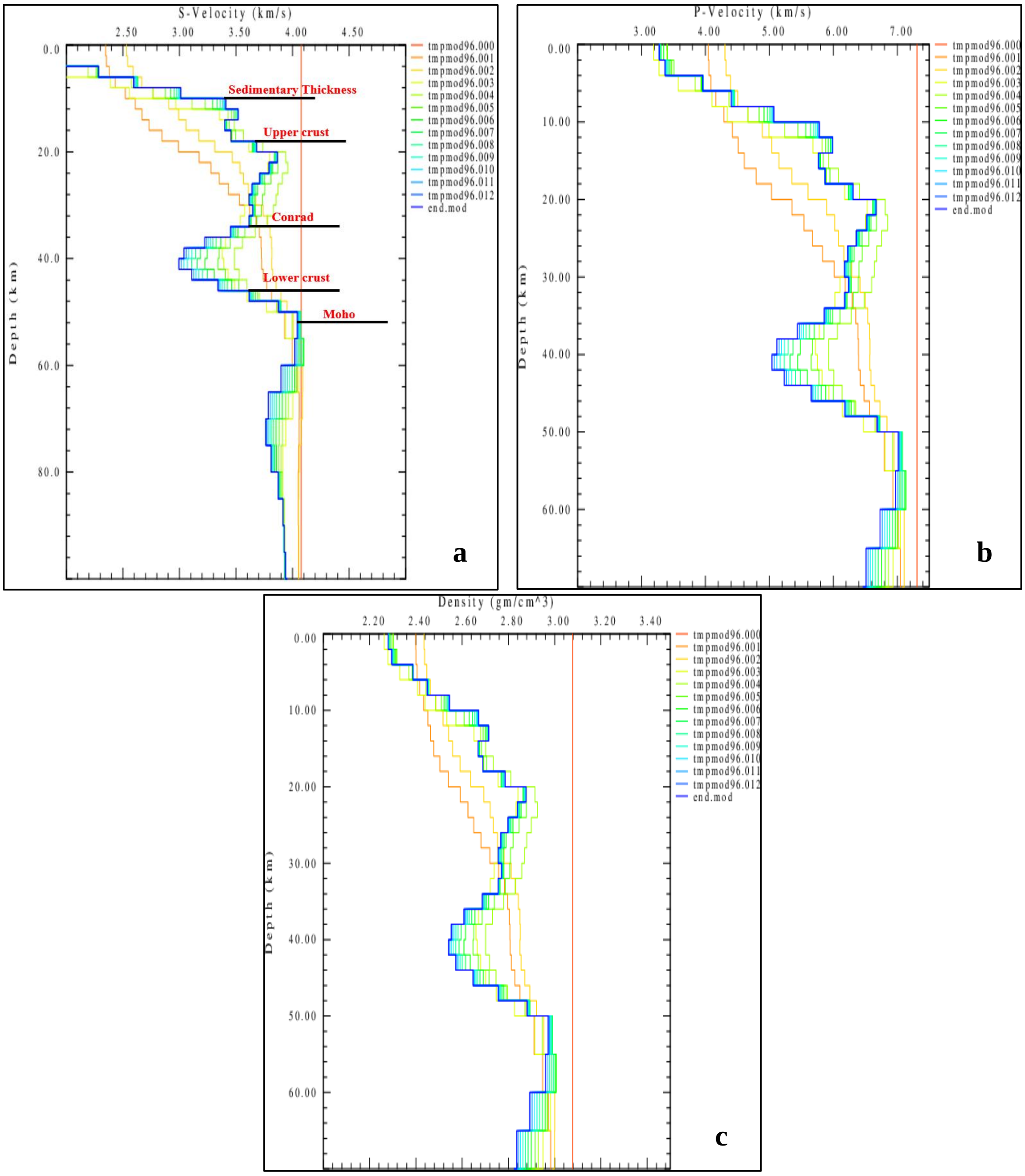

Figure 12. Crustal velocity model beneath the KUT1 station based on RFs: (a) S-wave velocity, (b) P-wave velocity, and (c) density profile.

The noticeable decrease of Vs at about 37 to 40 km depth in BGD1, KAR2, and KUT1 models can be attributed to several geological explanations. One of the explanations is the crust-mantle transition, where the velocity decrease may indicate the boundary between the lower crust and upper mantle or a significant change in rock composition, which may be caused by partial melting. The second reason could be the existence of a low-velocity zone (LVZ) that is generally formed due to high temperature, fluid accumulation, or partly molten material. If the region is tectonically active, the LVZ could signify hydrated rocks or weak zones that control the mechanical behavior of the crust. Additionally, the reduction in velocity may be attributed to the tectonic impact of the Zagros collision. Iraq lies near the Arabian–Eurasian plate boundary, where active compression may have led to processes such as delamination, crustal flow, or the formation of a ductile weak zone (Ali et al. 2014). Another plausible explanation is a shift from a typical Moho discontinuity, in which the crust-mantle boundary is distinct and not a gradational one, resulting in a gradual decrease in velocity over a depth interval. In addition, fluids or magmatic activity could be responsible, as deeply buried fluid reservoirs or partially molten material at the crustal base can reduce Vs values significantly. Overall, this pattern suggests a weakened, ductile zone in the lower crust, possibly caused by thermal softening, fluid movement, or partial melting over time. Comparing the results obtained for KAR2 and BGD1 with previous studies highlights both consistency and minor variation. At KAR2, the sedimentary thickness was estimated at approximately 10 km, slightly lower than the 12 km reported by Rafea et al. (2023). This difference may be due to variations in data resolution, inversion parameters, or the distribution of teleseismic events used in the analysis. For BGD1, the sedimentary thickness was about 8 km, closely aligning with the 6–8 km range reported by Gök et al. (2008) for the Baghdad station. These comparisons support the reliability of the RF inversion approach used in this study and suggest that the observed crustal variations across the Mesopotamian Plain are shaped by both regional tectonic processes and sedimentation history.

5. Conclusion

In this study, we provide an extensive examination of the crustal structure beneath three seismic stations, BGD1, KAR2, and KUT1, in central Iraq using the RF technique. By using an iterative time-domain deconvolution algorithm and inversion techniques, we delineated the subsurface velocity structure and identified the principal seismic discontinuities, including the Conrad and Moho boundaries, which are shown in Figures 9~11. The results reveal significant variations in crustal thickness and velocity profiles for the studied stations. The Moho depth was estimated to be about 40 km beneath KAR2, 49 km beneath BGD1, and 52 km beneath KUT1, revealing regional differences in crustal composition and tectonic history. We found the sedimentary cover to be the thickest beneath KAR2 (10 km), followed by BGD1 (8 km) and KUT1 (10 km), revealing the complex geological structure of the Mesopotamian Foredeep. Future studies must be aimed at the addition of more seismic stations, the addition of ambient noise tomography, and combined inversions with gravity and magnetic data to better constrain the subsurface models. These efforts will enhance our knowledge of the lithospheric structure of Iraq and earthquake hazard analysis in the region.

Acknowledgments

I would like to express my invaluable gratitude and appreciation to Dr. Hanan Mahdi and Dr. Haydar Al-Shukri for their guidance, support, and encouragement. I'm also grateful to Muntadher Al-Kaabi for his insightful contributions and collaboration, as well as to Seismic Monitoring Laboratory members for their encouragement throughout this research. Their assistance has been instrumental in the success of my work.

Appendix

Appendix 1. List of teleseismic event samples collected at the EMSC site for use in RF analysis of the KAR2 and KUT1 stations.

Date	Time	Latitude	Longitude	Depth	Magnitude
2023-4-22	8:23:43	-5.29	125.54	10	6.3
2023-4-19	9:6:3	-5.94	149.63	43	6.3
2023-4-18	4:31:42	-22.37	179.42	564	6.6
2023-4-14	9:55:48	-6	112.06	633	7
2023-4-4	12:54:35	13.78	125.49	22	6.2
2023-4-3	3:6:56	52.86	158.43	92	6.5
2023-4-2	6:4:12	-4.27	143.09	73	7
2023-3-28	9:18:29	41.19	142.77	40	6
2023-3-27	10:19:16	-8.29	158.91	85	6.1
2023-3-16	12:56:2	-30.13	-176.22	22	7
2023-3-14	12:49:9	-5.39	146.85	214	6.3
2023-3-7	1:51:50	-3.17	150.63	10	6
2023-3-7	6:2:31	7.53	126.11	10	6
2023-3-4	6:41:16	-29.64	-178.7	150	6.9
2023-3-2	6:4:32	-15.33	166.49	10	6.5
2023-3-1	5:36:15	-4.81	149.52	599	6.5
2023-2-25	9:24:49	-6.06	149.8	38	6.2
2023-2-25	1:27:43	42.89	145.04	50	6.1
2023-2-23	8:2:48	3.38	128.09	95	6.3
2023-2-17	9:37:31	-6.55	132.07	10	6.1
2023-2-15	6:10:9	12.35	123.87	12	6.1
2023-2-13	9:18:8	-29.52	-177.97	374	6.1
2023-2-11	8:55:8	3.65	126.67	54	6
2023-2-1	10:44:45	7.76	126.06	10	6
2023-1-26	10:45:53	-30.27	-178.66	126	6
2023-1-18	6:6:14	2.71	127.07	46	7
2023-1-18	12:34:45	0.08	123.17	153	6
2023-1-16	4:49:53	29.02	139.31	418	6.3
2023-1-9	5:47:35	-7.08	129.97	104	7.6
2023-1-8	12:32:42	-14.86	166.89	26	7
2022-12-28	4:34:21	-21.24	171.4	10	6
2022-12-14	6:40:27	51.73	178.75	71	6.3

2022-12-4	7:24:13	-15.38	-173.14	10	6.7
2022-11-22	2:38:12	-9.85	159.59	10	6
2022-11-22	2:3:7	-9.78	159.62	10	7
2022-11-14	8:8:26	33.84	137.24	352	6.1
2022-11-14	5:4:12	-26.05	178.2	631	6.1
2022-11-12	7:9:14	-20.14	-178.32	591	7
2022-11-11	10:48:48	-19.19	-172.35	45	7.3
2022-11-9	10:14:34	-25.68	178.32	631	6.6
2022-11-9	9:51:3	-26.12	178.34	651	7
2022-11-9	9:38:42	-26.07	178.35	629	6.8
2022-10-25	2:59:1	17.63	120.89	10	6.4
2022-10-13	10:20:22	-4.8	153.51	80	6.4
2022-9-20	6:23:42	55.62	166.52	10	6
2022-9-18	6:44:17	23.22	121.36	17	6.9
2022-9-17	1:41:19	23.15	121.42	10	6.5
2022-9-14	11:4:7	-21.17	170.25	139	7
2022-9-10	11:46:58	-6.22	146.48	80	7.6
2022-9-10	12:5:14	-2.19	138.15	20	6.2
2022-9-9	11:31:49	-2.2	138.17	25	6.2
2022-9-2	10:39:51	-5.63	148.68	119	6.1
2022-8-14	9:4:47	-22.03	170.87	80	6.2
2022-8-14	1:44:17	-32.77	-178.93	10	6.4
2022-7-27	12:43:23	17.48	120.83	10	7
2022-7-11	9:10:48	-18.14	169.03	10	6
2022-6-30	6:40:38	19.03	121.34	47	6
2022-6-4	11:38:11	52.08	178.26	105	6.3
2022-6-4	1:7:26	-17.9	-175.07	237	6.3
2022-5-27	2:36:4	-8.3	127.11	42	6.2
2022-5-26	3:38:12	-22.59	172.16	15	6.4
2022-5-22	3:17:33	33.19	141.42	28	6
2022-5-22	7:6:27	-26.23	178.38	580	6.3
2022-5-21	9:50:47	13.96	120.66	128	6.1
2022-5-9	10:33:6	-3.37	146.31	10	6.3
2022-5-9	6:23:12	24.02	122.49	20	6.3
2022-4-28	1:21:14	-4	146.58	10	6
2022-4-20	9:57:43	7.02	126.91	26	6
2022-4-19	4:33:41	-21.38	-173.98	10	6
2022-4-19	1:23:8	7.24	126.88	31	6.1
2022-4-17	7:46:36	-15.67	167.85	206	6.1
2022-4-9	8:52:37	-16.25	166.83	10	6.3
2022-4-4	4:6:56	-17.38	167.95	31	6
2022-3-31	7:50:39	-22.59	170.82	10	6.4
2022-3-31	5:44:1	-22.49	170.44	10	7
2022-3-30	8:56:58	-22.55	170.54	10	6.9
2022-3-23	9:57:12	-15.1	167.44	127	6
2022-3-22	5:43:25	23.46	121.46	19	6.1
2022-3-22	5:41:39	23.41	121.57	30	6.7

2022-3-20	6:10:44	-28.9	-177.38	51	6.1
2022-3-19	9:24:24	-25.34	-176.33	36	6.3
2022-3-16	2:36:32	37.73	141.62	49	7.3
2022-3-16	2:34:27	37.7	141.68	60	6.4
2022-3-13	9:5:49	14.07	119.44	10	6.4
2022-3-7	5:34:17	-20.38	-178.36	566	6.1
2022-3-2	12:52:9	-30.14	-177.8	40	6.6
2022-2-16	8:21:6	-23.81	-180	520	6.8
2022-1-29	2:46:39	-29.61	-176.64	10	6.5
2022-1-27	6:40:6	-19.1	-176.38	10	6.2
2022-1-22	5:17:7	53.34	-166.79	51	6.2
2022-1-22	2:26:15	3.73	126.7	40	6
2022-1-21	4:8:37	32.77	131.87	41	6.3
2022-1-16	12:52:10	-6.43	154.8	409	6.1
2022-1-11	12:39:33	52.64	-168.15	16	6.5
2022-1-11	11:35:47	52.77	-167.93	21	6.8
2022-1-10	12:6:31	-33.85	179.64	10	6.1
2022-1-4	8:55:47	-4.78	125.06	549	6
2022-1-3	9:46:38	24.08	122.26	30	6.2
2022-1-3	2:9:46	-13.15	166.85	125	6

Appendix 2. List of teleseismic event samples collected at the EMSC site for use in RF analysis of the BGD1 stations.

Date	Time	Latitude	Longitude	Depth	Magnitude
2024-2-10	3:22:4.66	8.663	125.6622	10	6.1
2024-2-10	17:44:45.09	36.243	70.071	144.8	6
2024-2-12	11:19:34.95	22.062	142.885	237.9	6
2024-2-12	11:19:37.63	22.0178	142.7999	260.2	6.1
2024-2-14	11:40:22.12	11.0047	138.5725	14	6
2024-2-14	11:40:26.38	11.0122	138.6152	38.9	6
2024-2-25	4:15:0.39	41.132	78.513	10.2	6
2024-2-25	13:7:4.3	-7.3405	105.9282	34	6.1
2024-3-1	9:29:2.86	8.8616	126.74	42.4	6.1
2024-3-1	17:29:44.95	11.5105	57.6508	8	6
2024-3-2	23:9:54.19	28.8025	128.2279	165.4	6
2024-3-8	9:11:46.35	5.855	126.87	124.4	6.1
2024-3-8	9:11:47.1	5.861	126.9773	132.8	6
2024-3-13	18:56:15.38	-0.155	125.197	41.2	6.1
2024-3-14	15:14:37.65	37.129	140.982	56.4	6
2024-3-14	21:10:24.78	29.7971	-42.6608	10	6.1
2024-3-14	21:29:15.63	29.711	-42.777	19	6.2
2024-3-22	8:52:58.99	-5.8754	112.3646	9.5	6
2024-3-22	8:53:0.38	-5.891	112.386	10	6.1
2024-3-24	3:4:7.84	-9.4207	122.1832	62.2	6
2024-3-27	2:3:29.43	46.2911	153.2782	10	6.1
2024-3-29	7:12:49.41	37.4404	21.4489	38.8	6

2024-3-30	16:28:57.45	52.1143	178.3963	109	6
2024-4-1	19:24:36.67	40.1435	141.6984	73	6.2
2024-4-1	19:24:37.74	39.8576	141.4403	70	6
2024-4-2	9:54:36.19	16.983	144.81	33	6.1
2024-4-2	23:58:11.72	24.2945	121.6233	10	7.4
2024-4-2	23:58:12.17	23.8356	121.5976	40	6.8
2024-4-3	0:11:24.89	24.0742	121.8883	10.5	6.4
2024-4-3	0:11:27.77	24.003	121.726	20.4	6.7
2024-4-3	0:35:36.12	24.175	121.78	1.5	6.8
2024-4-3	1:9:37.06	24.174	121.766	10	6
2024-4-3	2:14:36.14	24.184	121.963	31.9	6
2024-4-4	3:16:30.31	37.7104	141.856	29	6
2024-4-4	3:16:32.31	37.7377	141.713	42.2	6
2024-4-5	11:1:10.36	19.15	145.518	204	6.8
2024-4-5	11:3:16.35	19.1103	145.3659	222	6.9
2024-4-5	12:45:33.03	26.571	96.98	15.8	6.1
2024-4-9	9:47:59.81	2.6982	127.0624	22	6.4
2024-4-9	9:48:4.72	2.8722	126.5413	19.5	6.5
2024-4-10	14:56:17.07	41.9596	82.6648	8	6.3
2024-4-15	22:38:56.82	29.4397	131.7622	7.6	6.1
2024-4-17	14:14:45.75	33.3516	132.1058	10	6.2
2024-4-17	14:14:46.69	33.2503	132.3647	32	6.3
2024-4-18	15:11:25.85	40.122	36.157	15	6.1
2024-4-22	18:26:52.85	23.7141	121.6599	9	6.2
2024-4-22	18:32:48.43	23.8586	121.5662	10	6.1
2024-4-23	0:4:5.24	23.7794	121.6664	12	6
2024-4-27	8:35:35.9	27.863	139.531	518.2	6
2024-4-27	16:29:45.12	-7.916	107.32	71	6.1
2024-4-27	16:29:50.64	-8.005	107.2798	59.7	6.3
2024-4-30	13:52:40.87	2.2997	126.767	20	6.1
2024-5-4	5:52:36.44	-1.15	-14.309	10	6
2024-5-5	18:33:11.02	-3.3167	130.9618	16	6
2024-5-10	7:0:18.19	24.1885	121.9049	11.3	6.1
2024-5-19	9:35:24.66	52.0681	-170.912	28	6.2
2024-5-20	5:10:23.64	40.24	77.05	28.8	6
2024-5-23	11:27:3.21	-37.206	47.68	10	6
2024-5-28	11:52:40.25	2.8091	95.6066	21	6
2024-5-31	15:46:9.81	-43.3059	41.7226	10	6.1
2024-6-1	0:46:38.48	34.1381	86.3128	20.7	6.1
2024-6-1	0:46:40.0	34.1	86.1	34.5	6
2024-6-2	21:31:39.38	37.4476	137.2681	9	6
2024-6-5	2:20:27.14	-3.6756	100.6221	19	6
2024-6-5	2:20:42.53	-1.117	99.639	33	6.2
2024-6-6	11:7:53.35	50.1126	147.684	619.6	6
2024-6-12	17:1:18.27	4.5574	126.5021	13	6
2024-6-12	17:1:20.86	4.3762	126.4544	39	6
2024-6-14	4:26:48.66	-30.9404	-13.4721	10	6

2024-6-14	4:26:49.0	-31.1	-13.4	10	6
2024-6-14	9:51:55.82	-31.1899	-13.3185	10	6
2024-6-15	13:8:14.67	3.1837	127.2673	45.8	6.1
2024-6-15	13:8:16.68	3.1657	127.3267	63.7	6
2024-7-7	11:55:34.11	55.5772	162.1534	53	6.4
2024-7-7	20:1:12.29	26.8957	138.8289	546	6.1
2024-7-7	20:1:28.17	27.5232	137.6626	678.7	6.3
2024-7-7	20:15:49.81	55.6433	162.0058	74	6
2024-7-10	4:55:41.78	-53.3092	25.3481	4	6.3
2024-7-10	15:32:42.67	-5.4067	101.0211	9	6
2024-7-11	2:12:12.87	6.0547	122.9297	10	7.1
2024-7-11	2:13:18.77	6.099	123.147	638.8	6.5
2024-7-11	6:57:28.11	-20.4224	119.0515	10	6.6
2024-7-18	11:7:36.17	33.553	140.119	101.8	6
2024-7-18	15:1:25.53	-5.084	101.144	19	6
2024-7-19	3:13:47.57	52.2226	-171.02	38.2	6
2024-7-25	20:32:17.72	-7.407	128.615	144.5	6
2024-7-28	4:35:16.39	14.8365	108.2087	30.9	6
2024-8-2	22:23:2.21	8.254	126.671	29	6.6
2024-8-2	22:31:8.98	8.169	126.784	26	6.5
2024-8-3	4:20:28.0	8.189	126.765	24	6.2
2024-8-8	7:42:54.99	31.7915	131.6023	24.2	7.3
2024-8-9	14:5:10.87	35.529	22.358	10	6.1
2024-8-10	3:28:32.58	47.223	144.793	400.5	6.4
2024-8-15	23:35:54.0	23.7	121.8	10.7	6.3
2024-8-15	23:35:54.1	23.866	121.73	10	6
2024-8-17	19:10:25.72	52.956	159.8856	21.6	6.2
2024-8-17	19:40:0.35	53.0445	159.7972	33.1	6
2024-8-17	20:52:49.92	-6.6778	127.9976	332.6	6
2024-8-21	23:30:34.31	52.915	160.071	23.7	6
2024-8-26	0:17:5.13	1.026	126.3823	35.8	7.1
2024-8-26	1:32:2.62	52.907	159.548	55.4	6.7
2024-8-26	4:11:38.37	38.0154	-9.4907	10	6.2
2024-8-30	4:24:23.44	52.938	160.183	29.5	6
2024-9-2	0:39:36.62	4.568	96.31	10	6.1
2024-9-11	7:28:3.98	31.294	70.621	35.2	6.1
2024-9-13	23:3:41.46	29.834	130.864	29	6.1
2024-9-18	0:25:12.43	-25.8089	47.1856	0	6.5
2024-9-18	12:8:17.28	31.9107	117.6368	10	6.1
2024-9-23	19:51:3.08	-0.045	122.835	149.4	6
2024-9-23	23:14:20.77	31.516	139.889	10	6
2024-9-26	7:1:9.54	42.7876	145.0134	43.6	6.2
2024-9-26	19:19:29.49	-17.198	66.597	10	6.1
2024-9-30	12:21:58.15	53.019	160.114	31.1	6.1

References

Abdelwahed, Mohamed F. 2012. "SGRAPH (SeismoGRAPHer): Seismic Waveform Analysis and Integrated Tools in Seismology." *Computers & Geosciences* 40:153–65.

Abdulnaby, Wathiq, Hanan Mahdi, and Haydar Al-Shukri. 2012. "Crustal Structure from Joint Inversion of Receiver Function and Surface Wave Dispersion beneath Duhok, NW Iraq." In *Istanbul, 2012-International Geophysical Conference and Oil & Gas Exhibition*, 1–4. Society of Exploration Geophysicists and The Chamber of Geophysical ….

Abdulnaby, Wathiq, Khalil Motaghi, Esmaeil Shabanian, Hanan Mahdi, Haydar Al-Shukri, and Rengin Gök. 2020. "Crustal Structure of the Mesopotamian Plain, East of Iraq." *Tectonics* 39 (11): e2020TC006225.

ABERA, BIRHANU. 2016. "An Inversion Model of Receiver Function for Moho Depth Determination Beneath Locations of the Ethiopian Seismic Network Stations and Their Surroundings." *Addis Ababa University*.

Ahmad, Omar Q, and Wathiq G Abdulnaby. 2023. "Crustal Structure of Sulaymaniyah Area, NE Iraq from Joint Inversion of Receiver Function and Surface Wave Dispersion Analyses Using SLY1 Station." *The Iraqi Geological Journal*, 235–47.

Albakr, Majid A, Najah Abd, Ali Ramthan, Salar S Hasan Al Karadaghi, Wathiq Abdulnaby, and Ghazi H Al-Sharaa. 2022. "Shear Velocity from Seismic Ambient Noise to Determine Crustal Structure and Re-Fitting Rock Physics Modeling in Dhafriyah and Kumaite Oil Fields: Ambient Noise and Rock Physics Modeling." *The Iraqi Geological Journal*, 51–65.

Ali, Sarmad, Mohammad Mohajjel, Khalid Aswad, Sabah Ismail, Solomon Buckman, and Brian Jones. 2014. "Tectono-Stratigraphy and Structure of the Northwestern Zagros Collision Zone across the Iraq-Iran Border."

Al-Jabory, Asmaa N, and Emad Abdulrahman. 2024. "A Coda-Duration Magnitude Scale for the Mesopotamian Seismological Network in Iraq." *The Iraqi Geological Journal*, 159–74.

Al-Jabory, Asmaa Najim, and Emad Abdulrahman Al-Heety. 2024. "Duration Magnitude Scale for Anbar Seismic Station (ANB1), Iraq." *Journal of the University of Anbar for Pure Science* 18 (1).

Ariyanto, P, S Ariwibowo, A Wijaya, and R Pratama. 2020. "Crustal Structure Beneath KLNI Station in Lombok Island Based on Teleseismic Receiver Function." In *Journal of Physics: Conference Series*, 1491:012055. IOP Publishing.

Cassidy, John Francis. 1991. "Teleseismic Receiver Function Analysis of the Crust and Upper Mantle of Southwestern British Columbia." *University of British Columbia*.

Fouad, Saffa F A. 2015. "Tectonic Map of Iraq, Scale 1: 1000 000, 2012." *Iraqi Bulletin of Geology and Mining* 11 (1): 1–7.

Ghalib, Hafidh A A, Matthew S Sibol, Youlin Chen, Robert B Herrmann, Ghassan I Aleqabi, Hrvoje Tkalcic, Bakir S Ali, Borhan I Saleh, Dawood S Mahmood, and Robert A Wagner. 2008. "SEISMIC VELOCITY MODELING OF NORTH AND NORTHEAST IRAQ USING RECEIVER FUNCTIONS."

Gök, Rengin, Hanan Mahdi, Haydar Al-Shukri, and Arthur J Rodgers. 2008. "Crustal Structure of Iraq from Receiver Functions and Surface Wave Dispersion: Implications for Understanding the Deformation History of the Arabian–Eurasian Collision." *Geophysical Journal International* 172 (3): 1179–87.

Helffrich, George, James Wookey, and Ian Bastow. 2013. *The Seismic Analysis Code: A Primer and User's Guide*. Cambridge University Press.

Jansson, Thomas R N. 2008. "Receiver Function Modeling: Modeling Local Subsurface Velocity Structures Using Multiple Diverse Algorithms." *Niels Bohr Institute, University of Copenhagen. Master's Thesis in Geophysics*.

Ligorría, Juan Pablo, and Charles J Ammon. 1999. "Iterative Deconvolution and Receiver-Function Estimation." *Bulletin of the Seismological Society of America* 89 (5): 1395–1400.

Linang, Harry Telajan. 2023. "Crustal Structure and Tectonics of Borneo and Sulawesi: Results from Receiver Function Analysis and Virtual Deep Seismic Sounding."

Liu, Huafeng, and Fenglin Niu. 2012. "Estimating Crustal Seismic Anisotropy with a Joint Analysis of Radial and Transverse Receiver Function Data." *Geophysical Journal International* 188 (1): 144–64.

Ortega, Víctor, and Luca D'Auria. 2022. "Imaging the Crust and the Upper Mantle of Cumbre Vieja Volcano (La Palma, CanaryIslands) through Receiver Function Analysis." In *EGU General Assembly Conference Abstracts*, EGU22-8183.

Pant, Mohan. 2015. "Receiver Function Analysis to Study Crustal Structure of the Northern Nepal And Tibetan Plateau."

Rafea, Huda F, Emad A Al-Heety, and Wathiq Abdulnaby. 2023. "Geological Implications of Crustal Thickness, Vp/Vs, and Poisson's Ratio Beneath the Western Mesopotamian Plain Edge, Iraq." *The Iraqi Geological Journal*, 276–89.

Rafea, Huda Farhan, Emad A Al-Heety, and Wathiq Abdulnaby. 2022. "Crustal Velocity Structure of Western Iraq from Inversion of Receiver Functions at Anbar Seismic Station."

Ramthan, Ali, Wathiq Abdulnaby, Najah Abd, Hanan Mahdi, and Haydar Al-Shukri. 2020. "Crustal Structure beneath Al-Refaei Seismic Station–Central Mesopotamia, Iraq, Using Receiver Function Technique." *The Iraqi Geological Journal*, 77–87.

Ryan, Jamie, Susan Beck, George Zandt, Lara Wagner, Estela Minaya, and Hernando Tavera. 2016. "Central Andean Crustal Structure from Receiver Function Analysis." *Tectonophysics* 682:120–33.

Sissakian, Varoujan K, Lanja H Abdullah, and Ala Ghafur. 2024. "Tectonic Framework of Iraq. A Critical Review and Discussion." *Journal of Asian Earth Sciences* 276:106342.

Torsvik, Andreas. 2015. "Receiver Function Analysis-Seismic Imaging of the Crust beneath TROLL Seismic Station in Queen Maud Land, Antarctica." Dissertation.

Vervaet, François, and Fiona Darbyshire. 2022. "Crustal Structure around the Margins of the Eastern Superior Craton, Canada, from Receiver Function Analysis." *Precambrian Research* 368:106506.

Wilson, David C. 2004. "Seismic Structure of the Crust and Upper Mantle in the Southwestern United States Using Teleseismic Receiver Functions." *New Mexico Institute of Mining and Technology*.

Zhong, Minyan, and Zhongwen Zhan. 2020. "An Array-Based Receiver Function Deconvolution Method: Methodology and Application." *Geophysical Journal International* 222 (1): 1–14.

Zhu, Lupei, and Hiroo Kanamori. 2000. "Moho Depth Variation in Southern California from Teleseismic Receiver Functions." *Journal of Geophysical Research: Solid Earth* 105 (B2): 2969–80.